

Measuring Vehicle Velocity in Real Time Using Modulated Motion Blur of Camera Image Data

Minyoung Lee, *Member, IEEE*, Kyung-Soo Kim, *Member, IEEE*, and Soohyun Kim

Abstract—In this paper, a novel sensor system is presented for estimating the velocity using a modulated motion blur. By moving a camera mounted on the vehicle body with a specific pattern when the vehicle is moving, the blurred image includes the information of the vehicle velocity of the camera itself. It will be shown that the inclinations of motion blur in a scene are directly related to the velocity vector of the vehicle and the modulation speed. The proposed approach invariant to the exposure time provides the magnitude and direction of the velocity vector with high accuracy and high reliability. In contrast to other approaches using a camera image, our approach requires only 256×192 [pixel], and the proposed algorithm is simple and fast. The efficacy of the proposed method is demonstrated through simulations and experiments. The experimental results present empirical evidence to support that the proposed system is robust to climate changes such as rainy or snowy weather. The proposed system is expected to be applicable to vehicular technologies such as the vehicle dynamics controlling system or the vehicle positioning system.

Index Terms—Computational camera, modulated motion blur (MMB), motion blur, velocity sensor, visual odometer.

I. INTRODUCTION

ACCURATE velocity estimation techniques are important for the maneuver performance of vehicles [1]. In cluttered environments, the accurate velocity of the vehicle is required to safely maneuver to avoid obstacles or other vehicles [2], [3]. Several approaches to obtain the vehicle speed have been reported in the literature. In [4], the extended Kalman filter, which requires high computing power, a fast acquisition rate, and a large dynamic range, is adopted. More recently, the standalone global positioning system (GPS) has provided a good methodology for estimating the vehicle speed [5]. However, it is known that the accuracy of the GPS signal and the stability of the satellite connection may be genetic problems. In practice, the speed estimation from the Hall effect sensors on the wheels is available, but the lateral speed cannot be obtained. It is noted that the lateral speed and the slip ratio between tires and the ground are needed to obtain the driving and braking performance [6]. Meanwhile, lateral speed estimation using a linear

vehicle model with measurable parameters, such as the yaw rate, steering angle, and longitudinal speed, is frequently used when controlling the vehicle attitude. There is, however, inaccuracy due to nonlinearity in cornering stiffness and forces [7].

Many approaches to estimate the vehicle position and velocity using a camera system known as visual odometry have been developed [8], [9]. Among these, many are based on feature matching or feature tracking [10]. The feature matching-based algorithms rely on the motion estimation between adjacent image pairs and the camera system [11]. The feature tracking-based algorithm detects features in the image and searches them in the images followed by a camera. The approach can be adopted when the magnitude of motion is small and when feature's appearance has small changes, compared to the appearance taken in the first image of the procedure [12]. Meanwhile, the visual odometry can be classified as monocular visual odometry (MVO) [13] or stereo visual odometry (SVO) [14] by means of the number of cameras used. In general, the MVO estimates the movements of the ground in the frames. These ground movements with the camera height and pitch are then used to estimate the camera motion in real scale. Typically, the performance of the SVO is better than that of the MVO since the depth information is an important factor to estimate the magnitude of a motion.

Having framed the basis of visual odometry, in the following, we describe more recent research. The recent studies often incorporate machine learning or map matching, inertial measurement units, and combinations of several visual odometry methods. In [15], a robust ego-motion estimation method based on convolutional neural networks (CNNs) was introduced with three different kinds of neural network architecture. The best features and the best estimators were selected correctly through an automated learning process with presupplied datasets. The robustness of the CNN-based algorithm was validated through experiments. Multispectral stereo odometry was proposed in [16]. Using a frequency-based detector, features in the scene were extracted and described by the spatial and frequency information. The motion of the camera was computed using a sliding window (windowed) bundle adjustment with Gauss–Newton optimization. To handle the driving scenes with large motions and rapidly changing imagery, the monocular structure from motion by multithreading the multiple methods was introduced in [17] and [18]. The multiple methods of ground plane estimation were combined by introducing “adaptive cue combination”, including a Kalman filter and machine learning. In [19] and [20], a probabilistic model for visual self-localizing for vehicles located on known road maps was proposed. An inference algorithm that accurately computes vehicle location is handled in real time by

Manuscript received March 11, 2016; revised June 14, 2016; accepted July 27, 2016. Date of publication August 15, 2016; date of current version May 12, 2017. This work was supported by the Brain Korea 21 PLUS Program. The review of this paper was coordinated by A. Chatterjee.

M. Lee is with the Cho Chun Shik Graduate School for Green Transportation, Korea Advanced Institute of Science and Technology, Daejeon 305-701, South Korea (e-mail: lighton@kaist.ac.kr).

K.-S. Kim and S. Kim are with the Department of Mechanical Engineering, Korea Advanced Institute of Science and Technology, Daejeon 305-701, South Korea (e-mail: kyungsookim@kaist.ac.kr; soohyun@kaist.ac.kr).

Color versions of one or more of the figures in this paper are available online at <http://ieeexplore.ieee.org>.

Digital Object Identifier 10.1109/TVT.2016.2600281

0018-9545 © 2016 IEEE. Personal use is permitted, but republication/redistribution requires IEEE permission.

See http://www.ieee.org/publications_standards/publications/rights/index.html for more information.

using distributed computation. However, these visual odometry methods still rely on the detection/extraction of the features in the scene. Thus, obtaining more accurate motion/location requires high computation power. For example, the machine-learning-based algorithm must be run with a high-performance central processing unit (CPU) with a graphics processing unit (GPU) to compute the camera motion within few milliseconds.

Meanwhile, despite that the motion blurred image contains information of the relative motion of the camera to the objects in a scene, fewer studies have attempted to estimate the motion using the motion blurred image compared with the number of studies on visual odometry. In [21], the pure translation of a camera in 3-D motion was estimated for indoor localization and this was validated by experiments. By showing the relationship between the blur information and the speed of an object, the speed of the object moving in a single direction was detected from the motion blur in a scene [22]. In [23], a fusion of two ways to measure the speed of a vehicle moving in the scene of a camera fixed in the road was introduced. First, the direction of the motion blur caused by the movement of the vehicle in a scene was detected by using the Radon transform. Second, the length of this motion blur was estimated in the frequency domain using a density curve. Finally, the speed of the vehicle was estimated by utilizing the image geometry. In [24], similarly, the entire image was divided into each part of the image to detect the speeds of multiple vehicles, and then, the Fourier transform was performed to estimate the lengths and directions of the motion blurs. However, these methods rely on a camera fixed to the road or focus on indoor localization. Therefore, those approaches are not applicable for vehicle navigation or the dynamics status estimation.

On the other hand, approaches modulating the camera lens or image sensor to reconstruct the motion-blurred image have been widely researched in the area of image processing. In [25], a 1-D motion blur removal system translating within its exposure following a parabolic displacement rule was proposed. A 2-D motion deblurring system with orthogonal parabolic displacement was proposed in [26]. The parabolic motion of the imaging system makes the point spread function (PSF) to be almost same, although the speeds of the objects in a scene are different. By using the back-and-forth motion of a galvanometer mirror, similarly, a real-time de-blurring system was proposed in [27]. However, research using the modulation of the camera system has not focused on the object velocity estimation but, rather, it has focused on deblurring.

The main contributions of the paper are as follows.

- 1) In contrast to other visual odometry, the proposed system uses only one frame of the camera and provides the lateral velocity vector between the ground surface and the vehicle directly. Moreover, the required computation power is slightly low since the required image resolution is less than 256×192 [pixel], and the algorithm is very simple.
- 2) In contrast to other methods using the motion blur effect with modulation, we propose motion blur modulation to estimate the velocity of a camera mounted on the vehicle body. To the best of our knowledge, no work has been done in this direction. In the paper, we propose a simple visual odometer for ground vehicles that estimates 2-D velocity vectors, including the longitudinal and lateral speeds

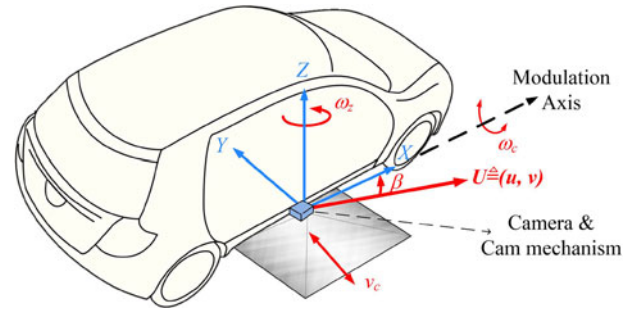


Fig. 1. Concept of the proposed system.

of a running vehicle. By modulating the motion of the camera heading toward the ground and mounted on the vehicle body, it will be shown that the velocity vector of the vehicle can be extracted from the modulated motion blurred images (MMBI). To define an optimal modulation speed of the camera and analyze the uncertainty in velocity estimation, a covariance analysis is performed, and through experiments, we validate the feasibility of the proposed method. Thus, the proposed method is a noteworthy, innovative contribution to vehicle dynamics control and navigation.

This paper is organized as follows. In Section II, the motion blur model during driving is presented, and the modulated motion blur (MMB) is introduced in terms of the velocity between the ground and the camera. The optimum modulation speed is also determined. In Section III, the proposed estimation algorithms are analyzed in the frequency domain. The effect of vibration with simulation is described in Section IV. The experimental results are provided in Section V. Finally, the conclusion and the discussion of future work follows in Sections VI and VII.

II. SPEED DETECTION USING MODULATED MOTION BLUR

A. Preliminaries

Let us consider the coordinate system O_{XY} fixed on the vehicle body, as shown in Fig. 1. The vehicle then may move with longitudinal velocity u and lateral velocity v , while rotating with yaw rate ω_z . It is noted that the side slip angle β is determined when the vehicle velocity $U \triangleq (u, v)$ is given. In addition, the camera is mounted on the vehicle, but the scene from the camera can be modulated in the y -axis with constant speed of v_c by rotating the cam mechanism with angular velocity of ω_c . On the other hand, the velocity vector defined by the vehicle center of gravity (COG) can be calculated by using the geometrical relationship between the camera mounting position and the COG.

For a brief explanation (see Fig. 2(a)), suppose that a light source (from target), P , moves along the X -axis, and the camera is at rest. The light through the pinhole is then marked at position x , on the image axis, which may be described by $x = f(X)$, where $f(\cdot)$ denotes the optical geometry function. Now, considering the 2-D motion of the target object (i.e., along the xy -axis) and the light intensity variation over time, the light intensity may be expressed by the function of x , y , and t , as shown in Fig. 2(b).

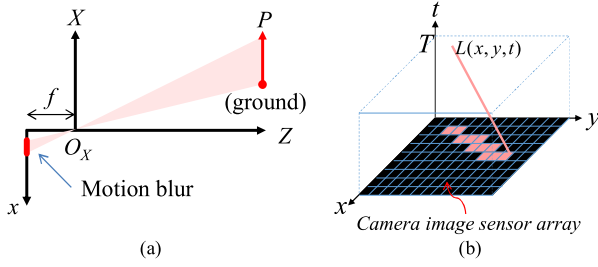


Fig. 2. (a) Pinhole camera model and (b) time-varying light field without intensity changes.

Hence, on a specific image cell, the image intensity can be described as follows [26]:

$$I(x, y) = \int_0^T L(x, y, t) dt \quad (1)$$

where T is the exposure time. The image intensity $I(x, y)$ can be modeled as a 2-D convolution integration of $L(x, y, t)$ with the kernel $k(x, y, t) = \delta(x - x_t) \cdot \delta(y - y_t)$ [26]:

$$\begin{aligned} I(x, y) &= \int_0^T L(x, y, t) dt \\ &= \int_0^T \int_{-\infty}^{\infty} \int_{-\infty}^{\infty} k(x - q, x - r, t) L_0(q, r) dq dr dt \end{aligned} \quad (2)$$

where $k(x, y, t)$ is the kernel that represents the trajectory of the light source during the exposure, and $L_0(x, y)$ is the initial light field. The kernel k then can be replaced by the PSF defined by [26]:

$$K(x, y) = \int_0^T \delta(x - x_t) \cdot \delta(y - y_t) dt \quad (3)$$

where positions x_t and y_t represent the trajectory of the light sources on the xy -axis, and δ is a delta function. Then, (2) becomes

$$\begin{aligned} I(x, y) &= I_0(x, y) \otimes K(x, y) \\ &= \int_{-\infty}^{\infty} \int_{-\infty}^{\infty} I_0(q, r) K(x - q, y - r) dq dr \\ &= \int_0^T \int_{-\infty}^{\infty} \int_{-\infty}^{\infty} I_0(q, r) \delta(x - x_t - q) \\ &\quad \cdot \delta(y - y_t - r) dq dr dt \end{aligned} \quad (4)$$

where $I_0(x, y)$ is an integration of the initial light field $L_0(x, y)$ over time, as follows:

$$I_0(x, y) = \int_0^T L_0(x, y) dt = L_0(x, y) T. \quad (5)$$

B. Modulated Motion-Blurred Image

Fig. 3 shows an example of a beam spot on the image sensor travel in x, y, t space. The result of the projection integration along the time axis is shown in Fig. 4. The static line in the figure is a trajectory of the light source in the image when we

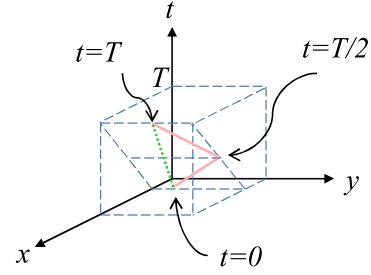


Fig. 3. Motion of a light source in the x, y, t space.

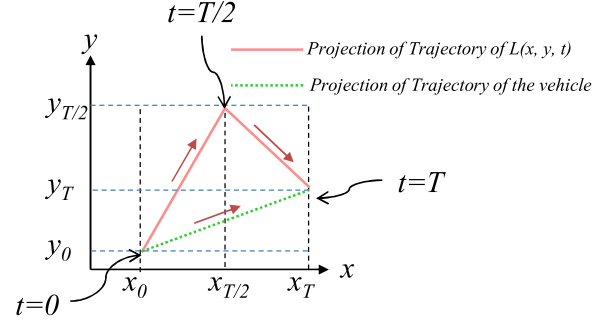


Fig. 4. Trajectories of the light source: recorded image.

modulate the camera in the y -direction. The magnitude of the modulation speed v_c is constant, and the direction of modulation is changed once at time $T/2$. The artificial camera position in y then returns to the origin at T . The green dotted line is the trajectory of the light source without modulation, which took place during exposure time T .

In Fig. 5(a), an asphalt image is shown as an ideal static image $I_0(x, y)$. When the vehicle is driving with velocity of u and v , the ideal image becomes motion blurred, as shown in Fig. 5(b). When an artificial modulation in camera with speed of v_c is added, an image with a specific blur pattern can be obtained, as shown in Fig. 5(c), which is called MMBI. From (3), therefore, the PSF becomes the trajectory of the light source, as shown in Fig. 3(b), and the trajectory can be represented by

$$y = \begin{cases} \frac{v_c + v}{u}(x - x_1) + y_1, & \left(\text{where } t \leq \frac{T}{2}\right) \\ -\frac{v_c - v}{u}(x - x_2) + y_2, & \left(\text{where } t > \frac{T}{2}\right) \end{cases} \quad (6)$$

where (x_1, y_1) and (x_2, y_2) are the starting points of the trajectory. Therefore, by using the inclinations given by $m_1 = (v_c + v)/u$ and $m_2 = -(v_c - v)/u$, one may calculate the velocity components as follows:

$$u = \frac{2}{m_1 - m_2} v_c \quad (7)$$

$$v = \frac{m_1 + m_2}{m_1 - m_2} v_c. \quad (8)$$

C. Determination of Modulation Speed

We have seen that the inclinations of motion blur are directly related to the velocity of the camera mounting point. However, there is uncertainty in the estimations of the inclinations due to

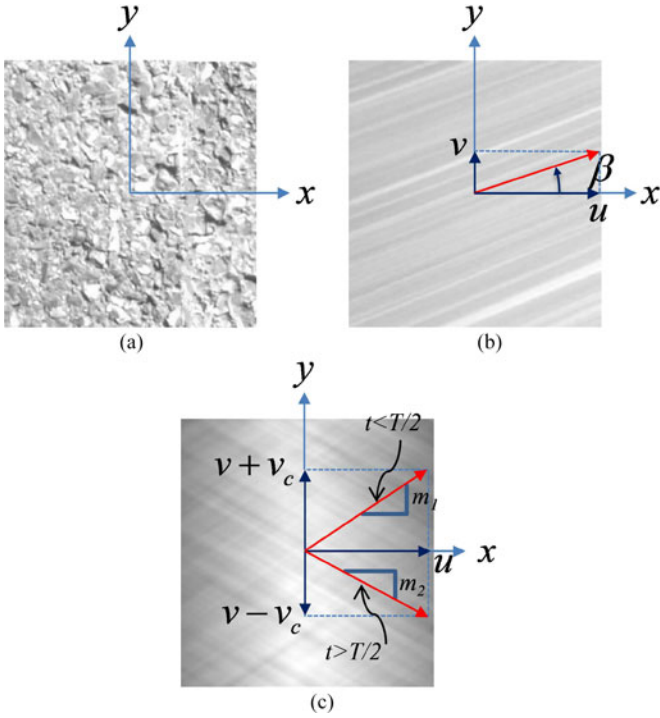


Fig. 5. Asphalt image taken by a camera. (a) Ground surface of asphalt. (b) Camera output when the vehicle is driving. (c) With camera modulation.

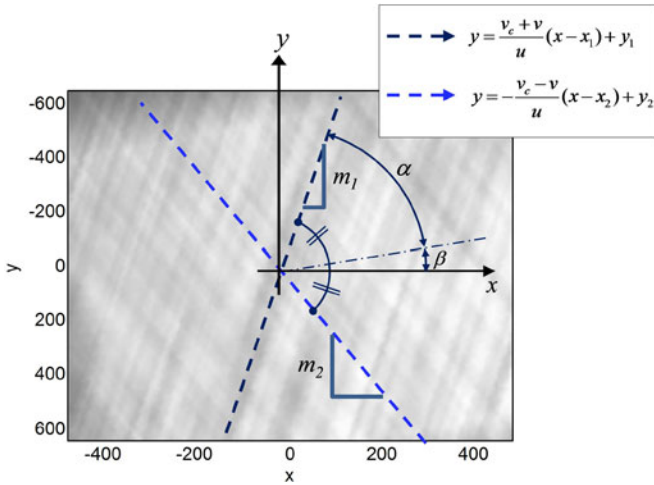


Fig. 6. Relationship between the vehicle velocity and the inclinations of the MMB.

disturbances such as the vibration of the vehicle. Therefore, it is acceptable to use the probabilistic model of the estimation algorithm to minimize the effect of the uncertainty in measurement. To simplify (7) and (8), the angles α and β are introduced as shown in Fig. 6:

$$\alpha = \frac{\tan^{-1} m_1 - \tan^{-1} m_2}{2} \quad (9)$$

$$\beta = \frac{\tan^{-1} m_1 + \tan^{-1} m_2}{2}. \quad (10)$$

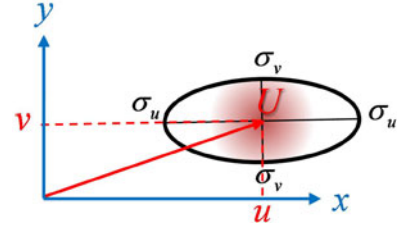


Fig. 7. Uncertainties in the estimation of velocity.

It is notable that the vehicle longitudinal speed u is much higher than the lateral speed v . Thus, we can assume that β is the vehicle side slip angle. Then, (7) and (8) become

$$u \cong \frac{1}{\tan \alpha} v_c \quad (11)$$

$$v \cong \frac{\tan \beta}{\tan \alpha} v_c. \quad (12)$$

Meanwhile, uncertainties such as $\sigma_m = [\sigma_{m_1} \sigma_{m_2}]^T$ in the measurement of $M = [m_1 \ m_2]^T$ exist. Similarly, $\sigma_\theta = [\sigma_\alpha \ \sigma_\beta]^T$ in the measurement of $\theta = [\alpha \ \beta]^T$, and the estimated velocity vector $U = [u \ v]^T$ has uncertainties about $\sigma_U = [\sigma_u \ \sigma_v]^T$, as shown in Fig. 7. The relationship between M and U is nonlinear; a Jacobian matrix F is required to verify the effect of uncertainty in the estimation of M [28]. The uncertainties of the measure of M are represented using the error covariance matrix C_M

$$C_M = \begin{bmatrix} \sigma_{m_1}^2 & \sigma_M \\ \sigma_M & \sigma_{m_2}^2 \end{bmatrix} = \begin{bmatrix} \sigma_{m_1}^2 & 0 \\ 0 & \sigma_{m_2}^2 \end{bmatrix} \quad (13)$$

(where the covariance σ_M is zero since the inclinations m_1 and m_2 in the image are generated independently at different times).

In addition, the uncertainties of the measure of θ are represented using the error covariance matrix C_θ

$$C_\theta = \begin{bmatrix} \sigma_\alpha^2 & \sigma_\theta \\ \sigma_\theta & \sigma_\beta^2 \end{bmatrix} \quad (14)$$

where σ_θ is a covariance of α and β . The uncertainties of the estimated angle are then represented using the propagated uncertainties, such as

$$C_\theta = F_M C_M F_M^T \quad (15)$$

where the Jacobian matrix F_M is defined as

$$F_M = \begin{bmatrix} \frac{\partial \alpha}{\partial m_1} & \frac{\partial \alpha}{\partial m_2} \\ \frac{\partial \beta}{\partial m_1} & \frac{\partial \beta}{\partial m_2} \end{bmatrix} = \frac{1}{2} \begin{bmatrix} \frac{1}{1+m_1^2} & -\frac{1}{1+m_2^2} \\ \frac{1}{1+m_1^2} & \frac{1}{1+m_2^2} \end{bmatrix}. \quad (16)$$

Similarly, the uncertainties of U are estimated using C_U :

$$C_U = \begin{bmatrix} \sigma_u^2 & \sigma_U \\ \sigma_U & \sigma_v^2 \end{bmatrix}. \quad (17)$$

The uncertainties of the estimated velocity vector are represented using the propagated uncertainties

$$C_U = F_\theta C_\theta F_\theta^T \quad (18)$$

where the Jacobian matrix F_θ is defined as

$$F_\theta = \begin{bmatrix} \frac{\partial u}{\partial \alpha} & \frac{\partial u}{\partial \beta} \\ \frac{\partial v}{\partial \alpha} & \frac{\partial v}{\partial \beta} \end{bmatrix} = v_c \begin{bmatrix} -\frac{1}{\sin^2 \alpha} & 0 \\ \frac{\tan \beta}{\sin^2 \alpha} & \frac{1}{\cos^2 \beta \tan \alpha} \end{bmatrix}. \quad (19)$$

To determine the optimal modulation speed $v_{c,\text{opt}}$ in terms of minimizing error propagation, we can rewrite (20) as follows:

$$\therefore F_\theta = v_c \begin{bmatrix} v_c + \frac{u^2}{v_c} & 0 \\ \left(v_c + \frac{u^2}{v_c}\right) \tan \beta & \frac{u}{\cos^2 \beta} \end{bmatrix}. \quad (20)$$

The cost function then can be set as a sum of elements in $F_\theta F_\theta^T$, and thus, the optimization problem becomes

$$\begin{aligned} v_{c,\text{opt}} &= \arg \min_{v_c \in \mathbb{R}} \frac{\sigma_u^2}{\sigma_\alpha^2} + \frac{\sigma_v^2}{\sigma_\alpha^2} + \frac{\sigma_v^2}{\sigma_\beta^2} \\ &= \arg \min_{v_c \in \mathbb{R}} (1 + \tan^2 \beta) \left(v_c + \frac{u^2}{v_c}\right)^2 = \arg \min_{v_c \in \mathbb{R}} \left(v_c + \frac{u^2}{v_c}\right)^2. \end{aligned} \quad (21)$$

Thus, the optimum modulation speed is

$$\therefore v_{c,\text{opt}} = \pm u. \quad (22)$$

In Fig. 8, the simulation results are shown to verify (22). Fig. 8(a) shows the effect of changing the modulation speed when the vehicle longitudinal velocity is varying. The error propagation ratio σ_u/σ_α is increased when v_c is not equal to u . In the simulation of the error propagation ratio σ_v/σ_α shown in Fig. 8(b), the lateral speed of the vehicle v varies from 5 to 90 km/h and the longitudinal speed u is increased from 0 to 100 km/h. Similarly, the error propagation ratio σ_v/σ_α is increased when v_c is not equal to u . On the other hand, the error propagation ratio σ_v/σ_β in Fig. 8(c) has no remarkable effect, although v_c is changed. It is notable that the minimum modulation speed should be considered to generate motion blur in the whole scene.

III. INCLINATION DETECTION METHODS

A. Inclination Detection From Images

The level of inclinations can be measured using line extraction methods such as the Hough transform or the Gabor filter with the angular variation. When the Hough transform is adopted, it is known that spurious peaks in the parameter space can be produced by nontarget shapes [29], and it is hard to find a proper grid size. The use of the Gabor filter involves a lot of computation power, due to the multiple convolution calculations required. Here, an inclination estimation algorithm in the frequency domain is presented. It is well known that the inclinations in the spatial domain correspond to a line orthogonal to

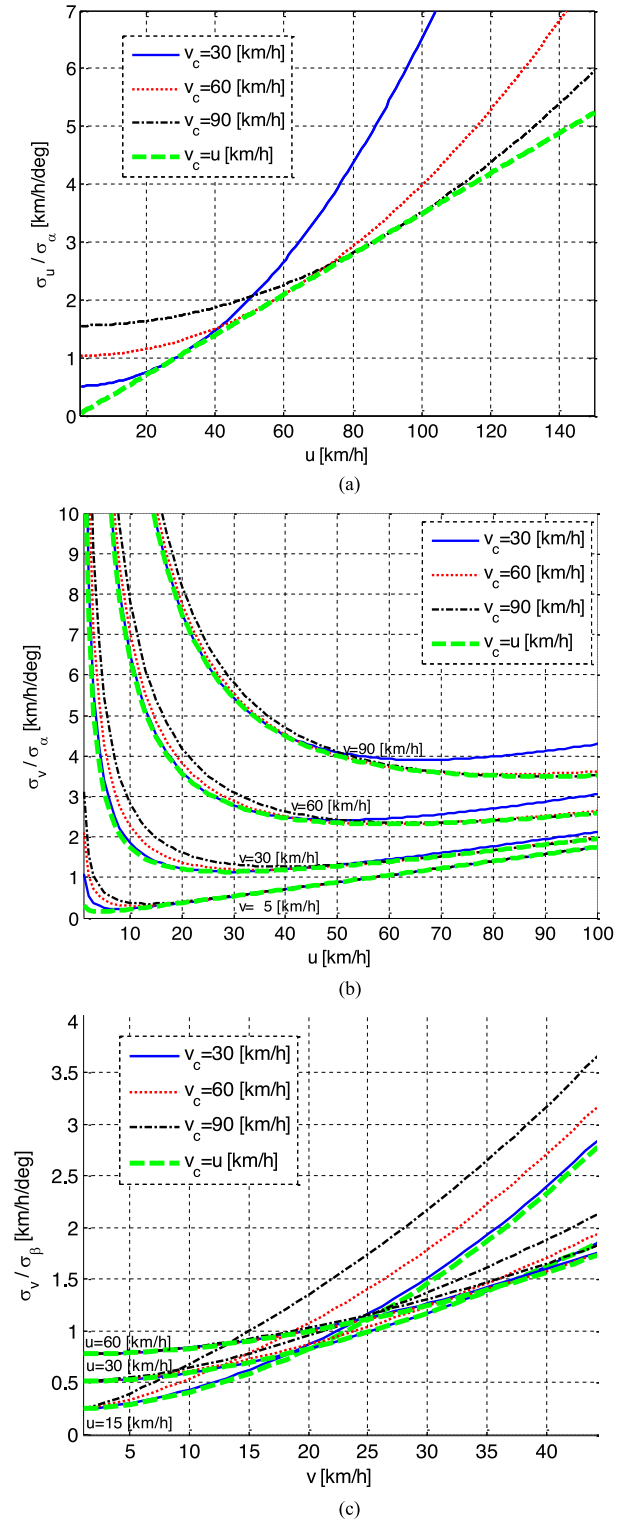


Fig. 8. Error propagation ratio. (a) $|\sigma_u/\sigma_\alpha|$. (b) $|\sigma_v/\sigma_\alpha|$. (c) $|\sigma_v/\sigma_\beta|$.

the inclinations in the frequency domain, and the magnitudes of the power spectra lying on the lines in the frequency domain are proportional to the number of corresponding lines in the spatial domain. Thus, the velocity can easily be estimated using the inclinations of the locally maximum power positions in the frequency domain. In this paper, accurate inclination estimation

methods in the frequency domain are presented in a twofold manner. First, an error minimization method using vehicle dynamics is presented. Second, a weighted regression technique to minimize the effect of the uncertainties caused by the smooth motion of the cam mechanism is demonstrated.

From (4), the motion blur can be represented as the multiplication of ideal image and PSF in the frequency domain [30]:

$$\begin{aligned}\hat{I}(\omega_x, \omega_y) &= \int_{-\infty}^{\infty} \int_{-\infty}^{\infty} I(x, y) e^{-2\pi i(\omega_x x + \omega_y y)} dx dy \\ &= \hat{I}_0(\omega_x, \omega_y) \hat{K}(\omega_x, \omega_y).\end{aligned}\quad (23)$$

The Fourier transform of PSF $\hat{K}(\omega_x, \omega_y)$ describing MMB in the frequency domain is defined as follows:

$$\begin{aligned}\hat{K}(\omega_x, \omega_y) &= \int_{-\infty}^{\infty} \int_{-\infty}^{\infty} K(x, y) e^{-2\pi i(\omega_x x + \omega_y y)} dx dy \\ &= \int_0^T \int_{-\infty}^{\infty} \int_{-\infty}^{\infty} \delta(x - x_t) \\ &\quad \cdot \delta(y - y_t) e^{-2\pi i(\omega_x x + \omega_y y)} dx dy dt \\ &= \int_0^T e^{-2\pi i(\omega_x x_t + \omega_y y_t)} dt \\ &= \int_0^{T/2} e^{-2\pi i\{\omega_x(x_0 + ut) + \omega_y[y_0 + (v + v_c)t]\}} dt \\ &\quad + \int_{T/2}^T e^{-2\pi i\{\omega_x(x_0 + ut) + \omega_y[y_0 + (v - v_c)t]\}} dt \\ &= \frac{e^{-2\pi A j}}{2\pi} \left[\frac{1}{B} (e^{-\pi B T} - 1) \right. \\ &\quad \left. - \frac{1}{C} e^{-2\pi C T j} (e^{\pi C T j} - 1) \right] j\end{aligned}\quad (24)$$

where $A = x_0\omega_x + y_0\omega_y$, $B = u\omega_x + (v + v_c)\omega_y$, and $C = u\omega_x + (v - v_c)\omega_y$.

Meanwhile, the power of the ideal image is amplified by the power of the PSF [31]:

$$\|\hat{I}(\omega_x, \omega_y)\|^2 = \|\hat{K}(\omega_x, \omega_y) \hat{I}_0(\omega_x, \omega_y)\|^2. \quad (25)$$

Thus, the powers of the positions located near the lines $(\omega_x + \frac{v_c + v}{u}\omega_y = 0, \omega_x - \frac{v_c - v}{u}\omega_y = 0)$ are amplified more than the powers of other positions. Therefore, estimating the velocity vector becomes a matter of finding out the positions of the locally maximum power in the frequency domain. In Fig. 9, a simulated power spectrum image with regression results is shown. The position of the locally maximum point is indexed, and then a first-order linear regression is conducted to determine the inclinations.

B. Boundary Constraints Considering Vehicle Dynamics

We have seen that the optimum modulation speed can decrease the effect of error in measurement. Therefore, it is important to minimize uncertainty in the estimation of α and β . To minimize the uncertainties of α and β , we need to consider

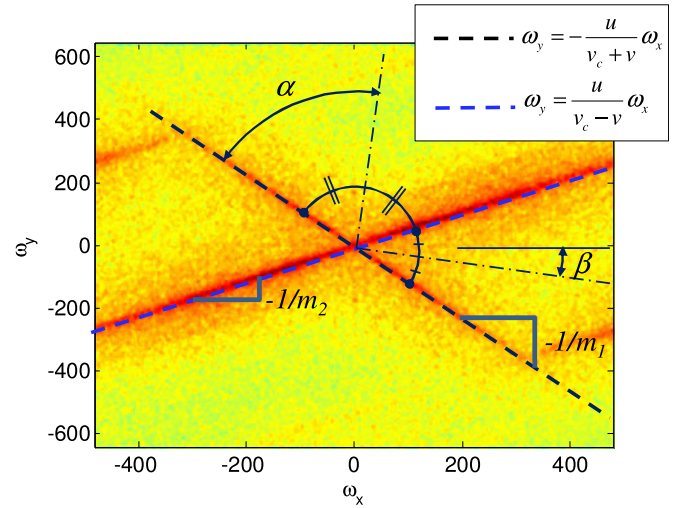


Fig. 9. Fourier transform of the MMBI and linear regression results for the locally maximum power position.

exhibiting the outliers in the regression algorithm. Thus, vehicle longitudinal dynamics is used for eliminating the outliers. We can represent the current time k th true value of u as

$$u_k = \frac{v_c}{\tan \alpha_k} = \frac{v_c}{\tan(\alpha_{k-1} + \Delta\alpha)} = u_{k-1} + \Delta u. \quad (26)$$

The k th true value of α is then represented as follows:

$$\alpha_k = \arctan\left(\frac{v_c}{u_{k-1} + \Delta u}\right). \quad (27)$$

Regarding the tire dynamics of the vehicle, the magnitude of the maximum deceleration rate is less than $1.3 \times g$. Our testing vehicle's maximum acceleration is less than $0.3 \times g$. Therefore, the boundary condition for the change of u can be set as follows:

$$-1.3g\Delta t < \Delta u < 0.3g\Delta t \quad (28)$$

where $\Delta t = 1/30$ [s], $g = 9.8$ [m/s²]; then

$$\therefore -0.4 < \Delta u < 0.1. \quad (29)$$

From the boundary constraints of u_k , the true value of α_k must be located within the range defined by

$$\arctan\left(\frac{v_c}{u_{k-1} + 0.1}\right) < \alpha_k < \arctan\left(\frac{v_c}{u_{k-1} - 0.4}\right) \quad (30)$$

$$\alpha_{k-1} - \Delta\alpha_L < \alpha_k < \alpha_{k-1} + \Delta\alpha_U \quad (31)$$

where

$$\Delta\alpha_L = \left| \arctan\left(\frac{v_c}{u_{k-1} + 0.1}\right) - \arctan\left(\frac{v_c}{u_{k-1}}\right) \right|$$

and

$$\Delta\alpha_U = \left| \arctan\left(\frac{v_c}{u_{k-1} - 0.4}\right) - \arctan\left(\frac{v_c}{u_{k-1}}\right) \right|.$$

Because the true value of α_{k-1} is unknown, a probability condition $\hat{\alpha}_{k-1}$ is considered:

$$P[\hat{\alpha}_{k-1} - \sigma_{\alpha, k-1} < \alpha_{k-1} < \hat{\alpha}_{k-1} + \sigma_{\alpha, k-1}] = 0.68. \quad (32)$$

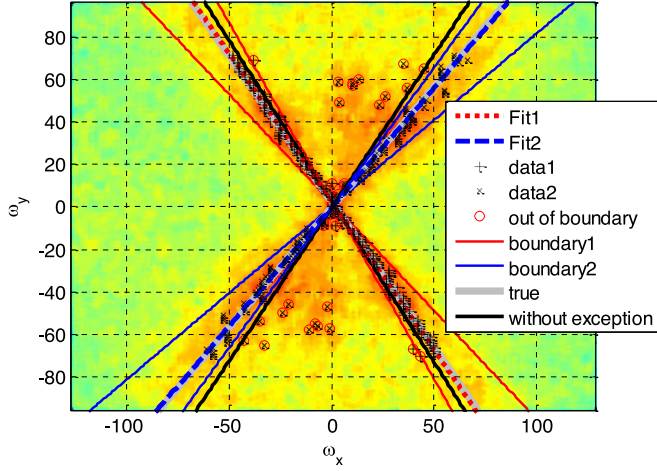


Fig. 10. Linear regression results of the simulation with boundary constraints.

Then, (30) becomes

$$\hat{\alpha}_{k-1} - \Delta\alpha_L - \sigma_{\alpha,k-1} < \hat{\alpha}_k < \hat{\alpha}_{k-1} + \Delta\alpha_U + \sigma_{\alpha,k-1}. \quad (33)$$

The same condition is applied to the estimation of β_{k-1}

$$\begin{aligned} \hat{\alpha}_{k-1} - \Delta\alpha_{L,k} - \sigma_{\alpha,k-1} - \sigma_{\beta,k-1} &< \hat{\alpha}_k \\ &< \hat{\alpha}_{k-1} + \Delta\alpha_{U,k} + \sigma_{\alpha,k-1} + \sigma_{\beta,k-1}. \end{aligned} \quad (34)$$

Note that the estimations of $\Delta\alpha_L$ and $\Delta\alpha_U$ have uncertainty, but we do not take this into account because larger boundary constraints cause the error to be increased.

The outliers lead to decreased reliability of the regression result. Therefore, disregarding the outliers can increase the reliability of the estimated value of the inclinations, as shown in Fig. 10. “Fit1” and “Fit2” are the regression results (using the data marked “+” and “x”) within the boundary constraints. The black lines “without exception” are the regression results using the data involving outliers (red circles), and thus, it does not fit the true line.

C. Weighted Regression

We have seen that regression within boundary constraints can decrease error compared to regression without outlier elimination. On the other hand, we have to consider some issues with the cam mechanism generating the MMB. In Fig. 11(a), the motion profile representing the modulation movement is shown. In Fig. 11(b), the PSF generated by the cam mechanism has a smooth change of direction when the time is near $T/2$. The smooth curvature causes the value of the power spectra to be distributed between the lines, as shown in Fig. 11(c). The energy distribution is proportional to the angle at origin $\pi/2 + \beta_{k-1}$. Hence, the weighting function w_s is set to be a line with vertical symmetry, as shown in Fig. 11(d). When the power is higher, the reliability of PSF is also higher. Therefore, we can set w_p to be the normalized power of each point. The problem then becomes weighted regression. We set W to be a diagonal

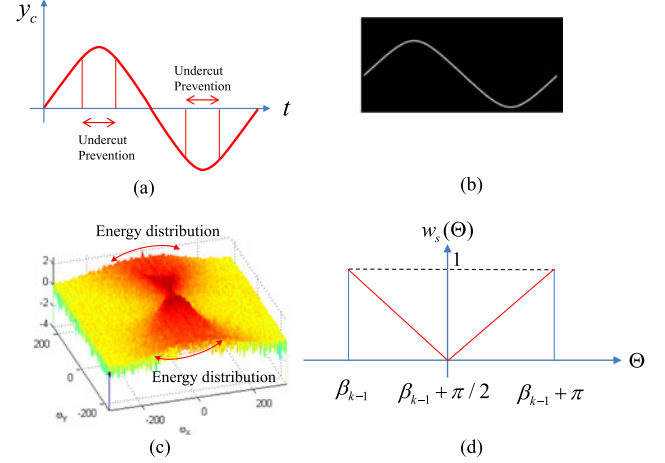


Fig. 11. (a) Motion profile with undercut prevention, (b) expected PSF, (c) power spectra of the PSF in frequency domain, and (d) weighting function (where $\Theta \triangleq \arctan(\omega_y / \omega_x)$).

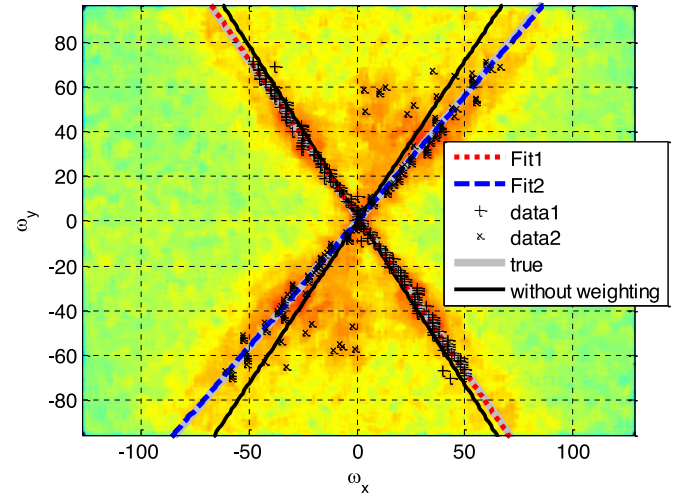


Fig. 12. Weighted regression result of the simulation.

matrix with diagonal elements equal to

$$w_i = w(\omega_{x,i}, \omega_{y,i}) \quad i = 1, 2, 3, \dots, n \quad (35)$$

where $w(\omega_x, \omega_y) = w_s(\omega_x, \omega_y) * w_p(\omega_x, \omega_y)$.

The weighted residual sum of squares is defined as follows:

$$S_w(\gamma) = \sum_{i=1}^n w_i (\omega_{y,i} - \omega_{x,i}^T \gamma)^2 = (\Omega_y - \Omega_x \Gamma)^T W (\Omega_y - \Omega_x \Gamma). \quad (36)$$

The weighted least square is then used to find estimates of Γ that minimize the weighted sum of squares of error:

$$\hat{\Gamma} = (\Omega_x^T W \Omega_x)^{-1} \Omega_x^T W \Omega_y. \quad (37)$$

In Fig. 12, the weighted regression results are shown as an example. “Fit1” and “Fit2” are the weighted regression results. The error is reduced compared to the linear regression without the weighting function, because the effects of the outliers are diminished. This is due to the rule of the weighting function we proposed.

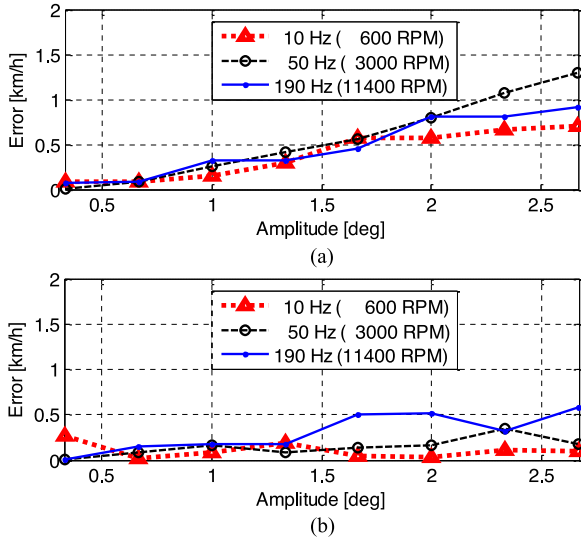


Fig. 13. Vibration effect on error. (a) Lateral velocity error $|e_u|$ and (b) longitudinal velocity error $|e_v|$.

IV. EFFECTS OF THE VIBRATION

A vehicle vibrates due to the engine operation, external disturbances by road roughness, and sound from loudspeakers. These vibrations can be classified as bounce, roll, and pitch [32]. The vibrations will affect the path of MMB. However, the bounce only affects the defocus blur in general and the pitch vibration does not affect the PSF when the vehicle is travelling at high speed. However, the roll vibration can increase the uncertainty in estimation. Fig. 13 shows the simulation results of MMB with roll vibration as an example. The amplitude of the vibration is increased 0.3° to 2.7° and the frequency is increased 600 to 11 400 r/min. We assume that the true value of the vehicle is 30 km/h and that there is no sideslip. The longitudinal velocity error $|e_v|$ and lateral velocity error $|e_u|$ are shown in Fig. 13(a) and (b), respectively.

Because the side slip angle is the bisection of the included angle of the MMB, the lateral velocity errors are less influenced by the changes of amplitude of the vibration. Meanwhile, the longitudinal velocity errors are increased when the amplitude is increased. Fig. 14 shows an example of a hazardous situation when a vehicle vibrates along the x -axis (rolling) with amplitude of 2.7° and frequency of 11 400 r/min. As shown in Fig. 14(d) and (e), the proposed algorithm well estimates the inclinations of the MMB, despite the large vibration that did not appear in the real situation. Moreover, our test vehicle has less than 0.5° amplitude of roll vibration in the experiments. Therefore, we ignored the effect of the vibration in the experimental results.

V. EXPERIMENTAL RESULTS

A. Hardware of the Proposed System

In order to verify the proposed sensor system, we designed a cam mechanism for generating MMB, as shown in Fig. 15(a)–(c). The motor and cam let the displacement of the ball joint create a triangular waveform at the desired acceleration. Be-

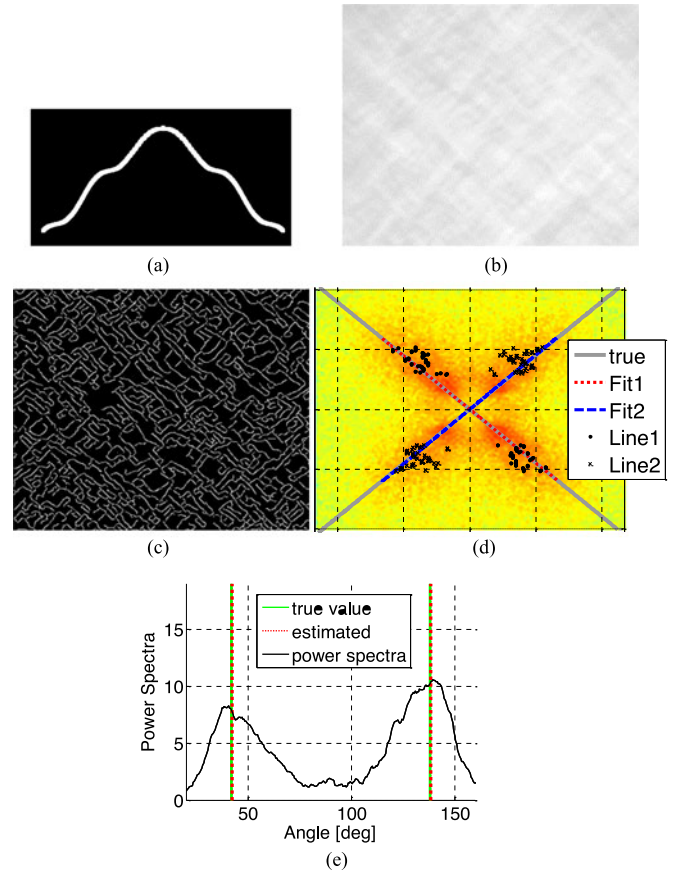


Fig. 14. Example of a simulation: 2.7° , 11 400 r/min: (a) PSF, (b) image, (c) edge, (d) power spectra with regression results, (e) and sum of power spectra along angular direction.

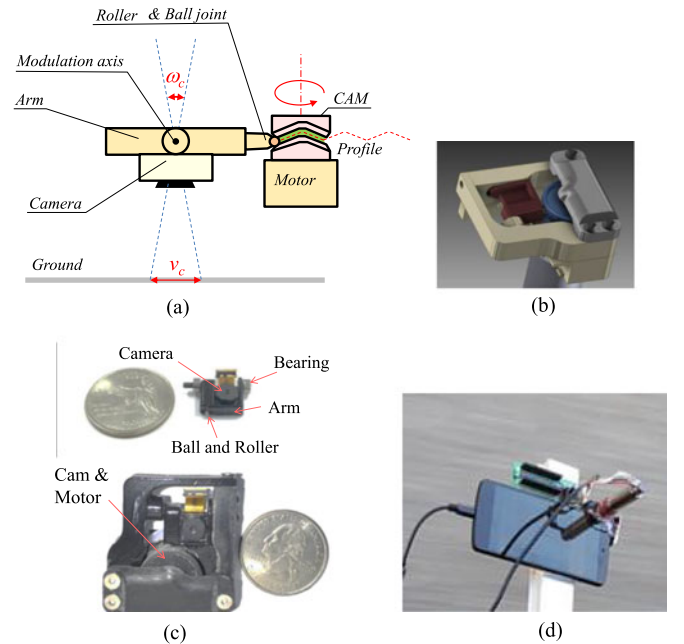


Fig. 15. (a) Concept of cam mechanism, (b) 3-D design, (c) 3-D printed cam mechanism, and (d) complete hardware set up used to evaluate the feasibility of the system.

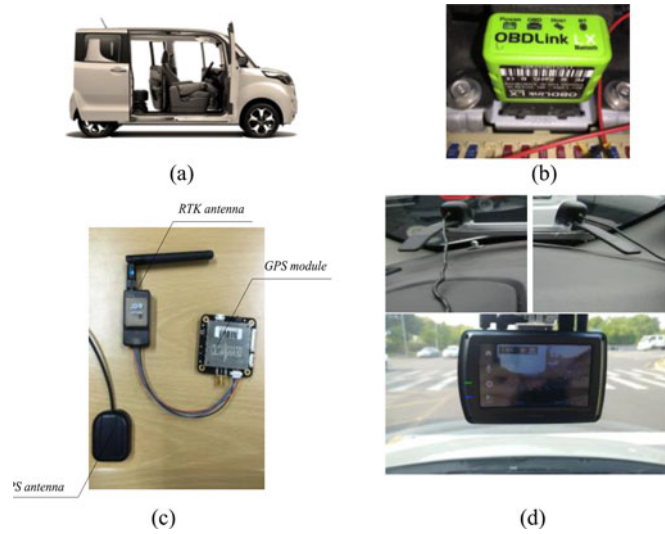


Fig. 16. (a) Test vehicle: 2013 KIA Ray. (b) OBDII Bluetooth module: OBDLink. (c) GPS receiver with *real-time kinematics* (RTK): Piksi. (d) Camera systems for the visual odometry (Libviso2) [33] for comparison.

cause the ball joint is mounted on a roller and arm, rotational movement is generated. The camera (the front facing camera "Google NEXUS 5") sits on an arm that rotates about the x -axis of the scene, and then, the scene moves around the y -axis. In our experiments, we assumed that the scene generated by rotational movement would be the same as the scene generated by pure translation with speed v_c . The hardware shown in Fig. 15(d) rotates the camera to evaluate the feasibility of the proposed method. In the experiment, we fixed the modulation speed to 25 km/h. The image was processed using an Android application and data were saved with measurable sensor data, such as acceleration, angular velocity, and rotation vector.

B. System Validation Tools

Fig. 16 shows the validation setup used to evaluate the feasibility of the proposed system. Fig. 16(a) shows a vehicle that has maximum acceleration of $0.3 \times g$ and maximum deceleration of $1.3 \times g$. The OBDII Bluetooth module shown in Fig. 16(b) was used to provide the wheel speed simultaneously. A GPS with a real time kinematics (RTK) module (shown in Fig. 16(c)) provides both GPS data and RTK data with reasonable accuracy. An Android application was developed to record experimental results simultaneously. Modulated motion-blurred video, three-axis accelerations, three-axis angular velocities, three-axis magnetic heading, rotation vector, GPS with RTK data, and vehicle-speed sensor (Encoder) data from the OBDLink were parsed and recorded in the application. Fig. 16(d) shows the camera system to compare the proposed method with monocular or SVO [33].

C. Computation Time

Table I shows the calculation time of MMB with a 256×192 [pixel] resolution image. The average time was calculated by measuring the time of a thousand loops with edge detection, discrete Fourier transform, and weighted regression.

TABLE I
CALCULATION TIME WITH DIFFERENT CPU AND OPERATING SYSTEMS

Model	Method	RAM [GB]	Average CPU Loads [%]	Average Time [msec]	operating system
Qualcomm MSM8974 Snapdragon 800	MMB	2	25	22.5	Android 5.0
Qualcomm MSM8996 Snapdragon 820	MMB	4	25	13.4	Android 6.0
Samsung Exynos5422	MMB	2	22	15.2	Ubuntu 15.04
Intel i7-6700HQ	MMB	16	30	6.3	Windows 7 64 bit
Intel i7-6700HQ	Libviso2 [33]	16	30	32.3	Windows 7 64 bit

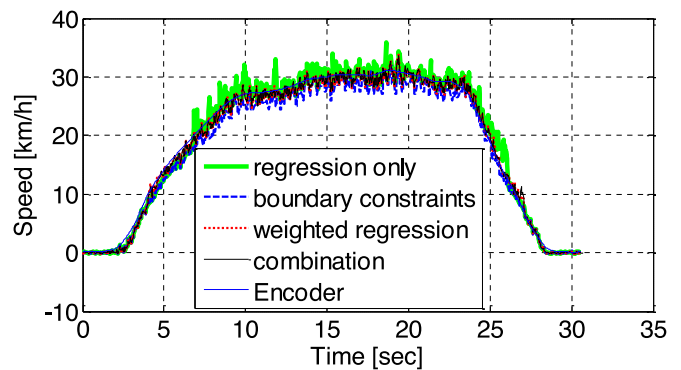


Fig. 17. Comparison of experimental results: speed.

TABLE II
COMPARISON OF THE REGRESSION TECHNIQUES

Methods	Average Error [km/h]	Standard Deviation of Error [km/h]
Regression	1.61	1.38
Boundary constraints	1.38	1.05
Weighted regression	0.98	0.90
Combination	0.94	0.88

The required time for calculation should be less than 33 [m·s] since we use a 30 FPS camera. Thus, all the CPUs we tested are suitable for covering the frame rate of the camera. In the experiment, we used a Qualcomm MSM9774 Snapdragon 800 system (Google Nexus 5).

D. Comparison of Regression Techniques

Fig. 17 presents the experimental results from the comparison of the various regression techniques described in Section IV. In Table II, the weighted regression method shows a remarkable decrease in error. The error calculated by the combination of the weighted regression method with incorporated boundary constraints has a SD of just 0.88 km/h. To consider the efficiency of the calculation, however, the following figures show the results from the MMB experiment, with weighted regression.

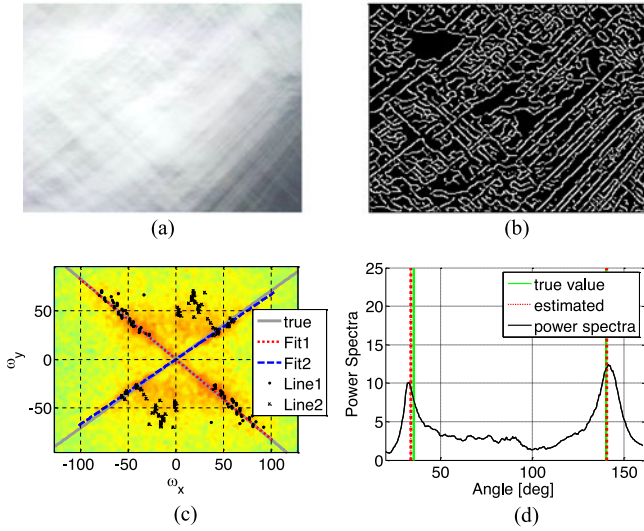


Fig. 18. MMBI from snowy ground surface. (a) Image taken, (b) edge of the image, (c) power spectra of the image with inclination detection, and (d) sum of power spectra in angular direction.

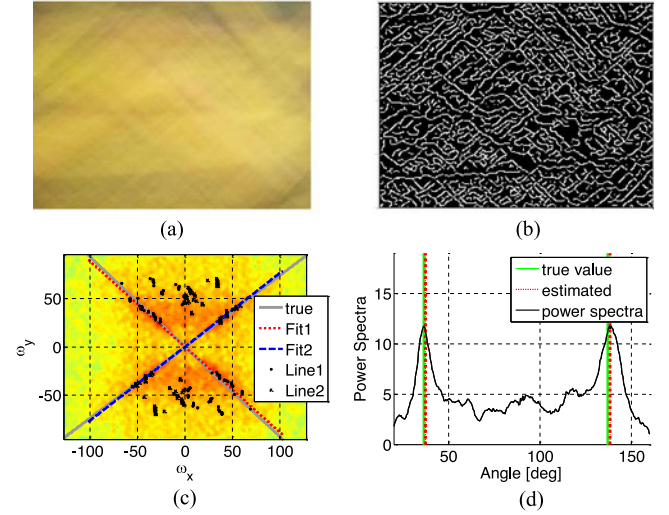


Fig. 20. MMBI with doubled centerline. (a) Image taken, (b) edge of the image, (c) power spectra of the image with inclination detection, and (d) sum of power spectra in angular direction.

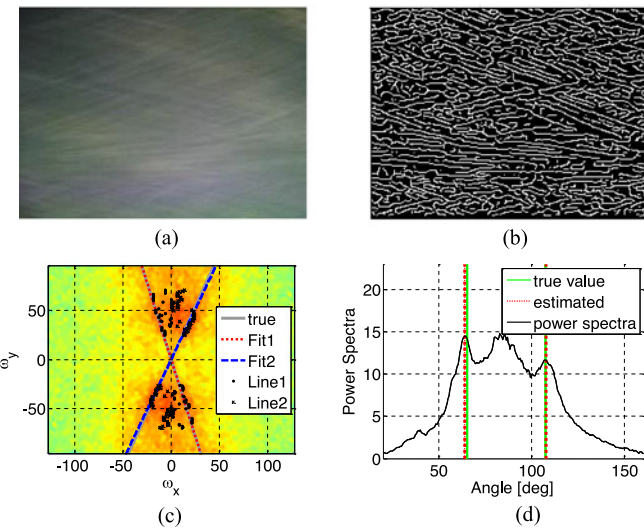


Fig. 19. MMBI from rainy ground surface. (a) Image taken, (b) edge of the image, (c) power spectra of the image with inclination detection, and (d) sum of power spectra in angular direction.

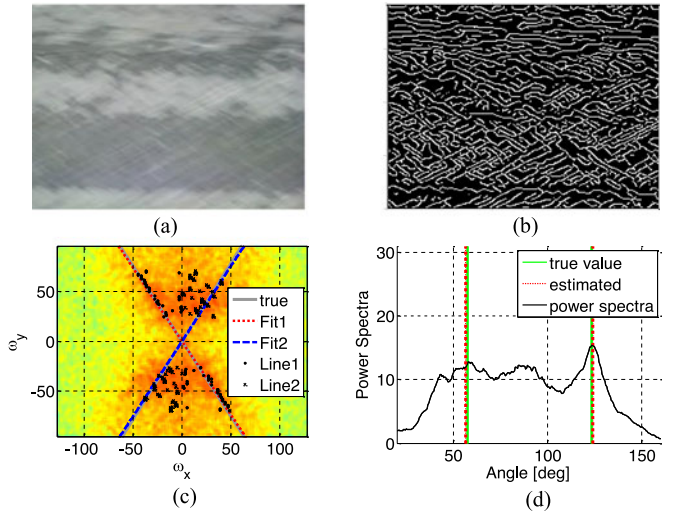


Fig. 21. MMBI with white ground paintings. (a) Image taken, (b) edge of the image, (c) power spectra of the image with inclination detection, and (d) sum of power spectra in angular direction.

E. Experimental Results

1) *Environmental Effects:* To examine the robustness of the MMB method against severe environments, examples are provided in Figs. 18 to 21. Fig. 18 shows an example frame from the camera in a snowy environment. Although the asphalt was covered with snow, the specific pattern was recorded in the image sensor, as shown in Fig. 18(a), and the edge-extracted image is provided in Fig. 18(b). The power spectra and its accumulation in the angular direction is shown in Fig. 18(c) and (d). Similarly, the results from the rainy environment are shown in Fig. 19. The motion blurs generated by the slow objects (e.g., falling/splashing waters) in a scene distribute the energy in the frequency domain, as described in the previous section. How-

ever, the particles are slower than the vehicle speed and the number of edges produced by the moving particles is lower than that generated by the ground surface. Thus, the proposed weighted regressing algorithm can reduce the effects. Thus, the inclinations for estimating the velocity are well extracted, as shown in Fig. 19(c) and (d). On the other hand, the scene can change rapidly when the vehicle is passing painted road surface, such as yellow centerlines and white ground paintings. As shown in Figs. 20 and 21, however, the results show the robustness of the proposed system.

Table III shows results of the environmental effects on the obtained image and extraction algorithm. In the rainy environment, it appears that the error is increased. However, the percentage error of the longitudinal velocity is almost the same. Meanwhile,

TABLE III
EXPERIMENTAL RESULTS OF THE ENVIRONMENTAL EFFECTS

Environment	u_{true} [km/h]	Inclination error		Angle error [degree]		Velocity error [km/h]	
		$ e_{m1} $	$ e_{m2} $	$ e_{\alpha} $	$ e_{\beta} $	$ e_u $	$ e_v $
Snowy	20	2.01	0.56	0.81	0.67	0.58	0.96
Rainy	68	2.24	1.30	0.59	0.58	2.00	4.73
White ground paintings	41	1.50	1.60	0.80	0.24	1.20	0.18
Doubled centerline	22	2.25	2.51	0.27	1.23	0.21	0.78

*Since the images are taken when the vehicle is coasting without steering, the true values of the longitudinal speed u_{true} are the same as the wheel speed, and the true values of lateral velocities v_{true} are assumed zero. There also exist the possibilities that unexpected side slip occurs when the images are taken.

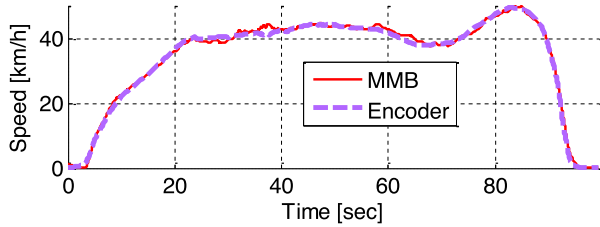


Fig. 22. Example of the speed estimation.

TABLE IV
ERROR OF THE LONGITUDINAL VELOCITY ESTIMATION

Speed Range [km/h]	Average Error [km/h]	Standard Deviation of Error [km/h]	Average Percentage Error [%]
0–20	0.35	0.33	1.72
20–40	0.73	0.23	2.01
40–60	0.97	0.36	2.15
60–80	1.42	0.50	2.03
80–100	2.13	0.95	2.35

the lateral velocity error in a rainy environment is increased, although the error of side slip angle $|e_{\beta}|$ is reasonable. Because of the error propagation ratios are increased when the longitudinal speed is high as described in Section II-B. It is notable that the modulation speed is fixed at 25 km/h. Therefore, the error can be reduced by driving with the optimum modulation speed.

2) *Longitudinal Velocity Estimation*: To examine the accuracy of longitudinal speed estimation, we conducted the experiments following an almost straight line 30 times with different speed profiles. Fig. 22 shows an example from the experiments to demonstrate the performance of the system in terms of estimating longitudinal speed. The detailed information of the errors is shown in Table IV. We assumed that the wheel speed value marked as “Encoder” is the true value. The deviation of estimates increased when the vehicle speed increased. This is because the uncertainties in the longitudinal velocity estimation increase as the speed increases. However, the percentage error is less than 2.5% of the true value.

3) *Lateral Velocity Estimation*: The accuracy of lateral velocity estimation is examined in indirectly by rotating the camera

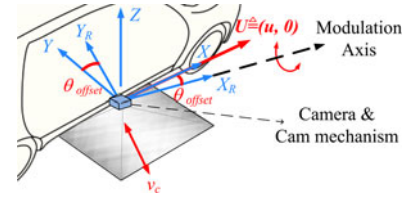


Fig. 23. Rotated MMB system about z-direction.

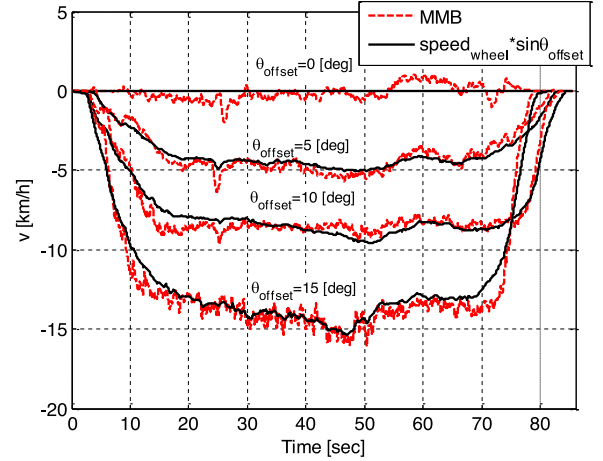


Fig. 24. Experimental results of the lateral velocity estimation.

TABLE V
ERROR OF THE LATERAL VELOCITY ESTIMATION

θ_{offset} [degree]	Average Velocity Error [km/h]	Standard Deviation of Error [km/h]	Average Side Slip Angle Error [degree]	Standard Deviation of Error [degree]
0	0.35	0.31	0.46	0.39
5	0.46	0.32	0.60	0.35
10	0.69	0.51	0.46	0.38
15	0.83	0.73	0.28	0.21

about θ_{offset} (z-direction). We can then assume that the vehicle is sliding with a slip angle of θ_{offset} (shown in Fig. 23). The true value of the lateral speed is calculated using the wheel encoder sensor and offset value: $v_{true} = v_{wheel} \sin \theta_{offset}$. Fig. 24 shows the experimental results, and Table V summarizes the error from the experiments. The average error of the lateral velocity is less than 0.83 km/h. The side slip error is less than 0.6°. The error is increased when the lateral velocity is large, as described in Section II.

4) *Localization*: To verify the effectiveness of our method for localization, experiments have been conducted, and the results with known ground truth data are shown in Figs. 25 and 26. The magnitude of speed $|U|$ and u, v is shown in Fig. 25(a) and (b), respectively. The angular information used to evaluate the position data is shown in Fig. 25(c). The localization results and radius are shown in Fig. 25(d) and (e). Fig. 25(f) shows the average θ error of the radius estimations compared with ground truth data. Here, “1” indicates the RTK method, and “2” and “3” indicate MMB and wheel encoder. The results of MVO

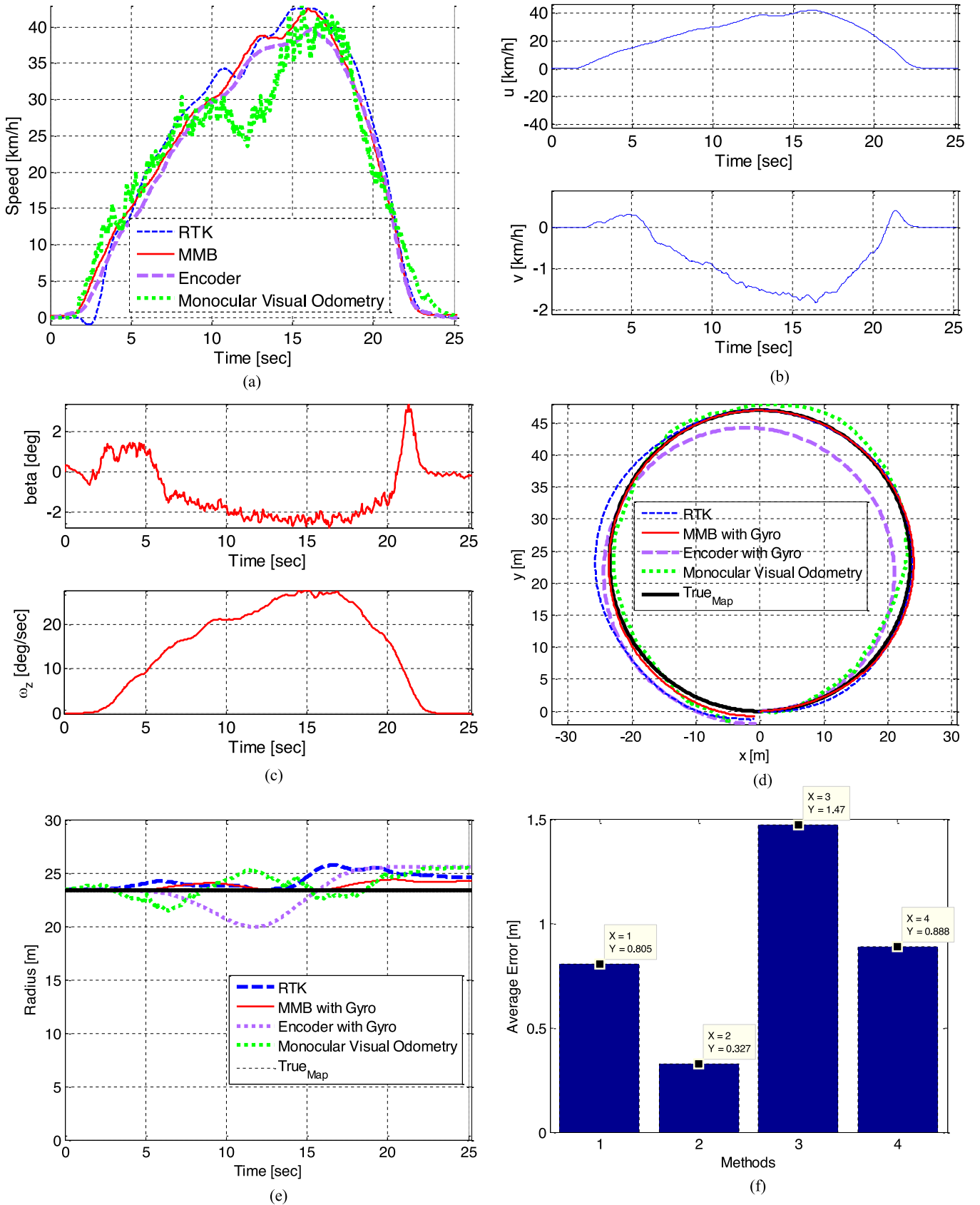


Fig. 25. Experimental results with ground truth data. (a) Speed, (b) velocity vector, (c) side-slip angle and angular velocity measured by MEMS gyro, (d) localization results, (e) radius, and (f) average error of radius.

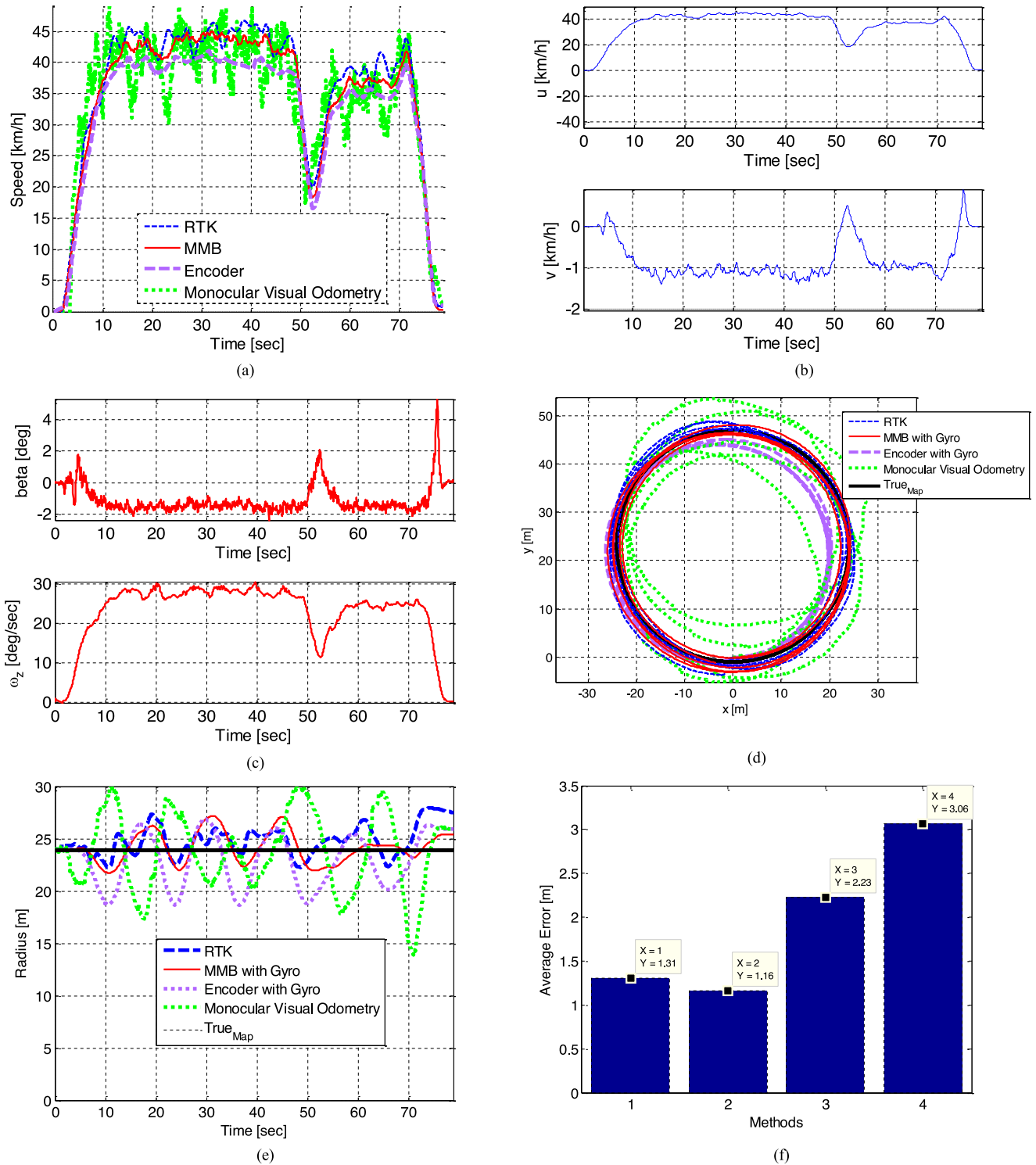


Fig. 26. Experimental results with ground truth data. (a) Speed, (b) velocity vector, (c) side-slip angle and angular velocity measured by MEMS gyro, (d) localization results, (e) radius, and (f) average error of radius.

[33], which are marked as “4,” are obtained by using the videos from the black box camera. The error of radius using MMB with a MEMS gyro sensor is less than that when using other methods. Similarly, Fig. 26 shows the experimental results with five rotations of the same trajectory. The sequence of the subfigures is the same as in Fig. 24. The error of radius estimation shown in

Fig. 26(f) is greater than that in Fig. 26(f). This is due to the integration of the velocity vector with angular velocity measured by the MEMS gyro allowing accumulation of the uncertainties in the estimation of velocity vectors.

The detailed localization performance was evaluated in urban roads. The RTK method was not available because we

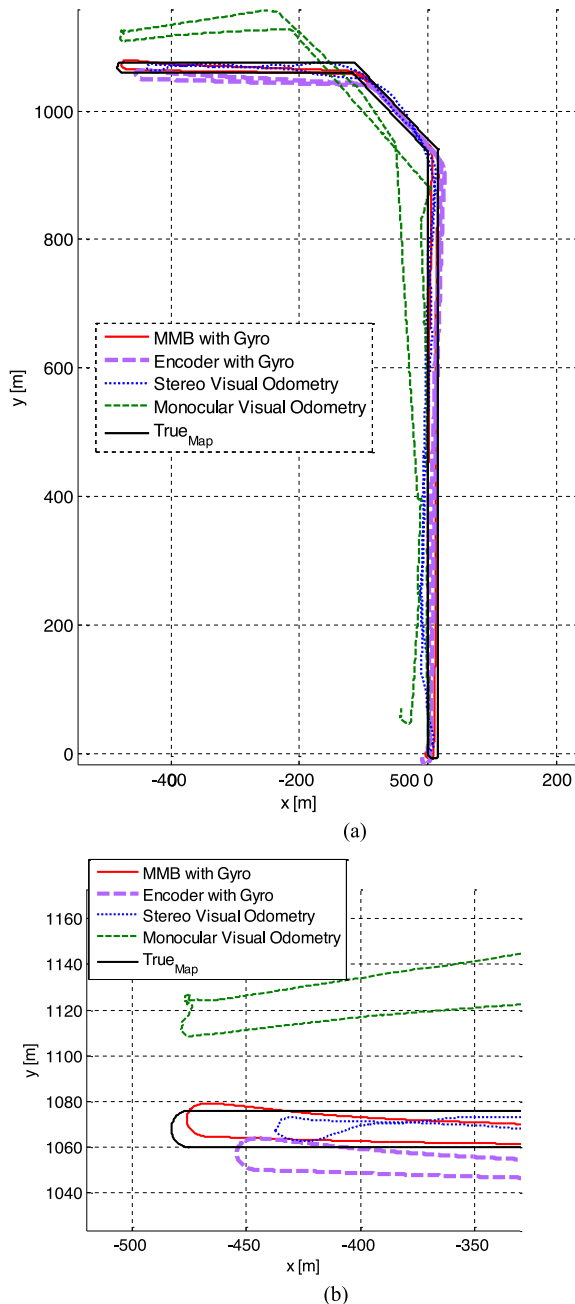


Fig. 27. Example from the localization results. (a) Localization results. (b) Zoom of the turning point.

drove more than 1 km from the starting point (distance limitation between the base RTK device). SVO [33] was performed to compare the localization performance. An example of the localization results is provided in Fig. 27. The total travel distance of the experiment is 2.9 km. Table VI presents more detailed errors of localization. The MMB has minimal error compared with SVO or MVO.

VI. CONCLUSION

In order to detect the vehicle velocity vector in 2-D motion, a novel sensor system using MMB has been newly devel-

TABLE VI
COMPARISON OF DEAD-RECKONING PERFORMANCE
(TRAVEL DISTANCE: 2.95 KM)

Methods	Average error [m]	Root Mean Squared Error [m]	Maximum error [m]
MMB	3.24	3.91	8
MVO [33]	24.22	31.59	82
SVO [33]	4.88	5.61	12
Encoder	5.88	7.35	18

oped and implemented. The motion blur model for the MMB is analyzed in the frequency domain. We proposed several algorithms to minimize the error in estimation and compared the obtained results with experimental results. It was shown that the weighted regression algorithm incorporating boundary constraints results in the least error deviation in estimation. The effectiveness of the proposed method for estimating the velocities and localization was validated by experiments. The longitudinal velocity error is less than 2.13 km/h and the lateral velocity error is less than 0.83 km/h. To our knowledge, there has been no research using a camera that has provided lateral velocity and that has achieved this level of error. The localization results are compared with MVO and SVO. The maximum localization error of our system was just 8 m for 3 km of total travel distance.

We have developed a reasonable simple real-time velocity measurement system, while simultaneously providing lateral velocity and longitudinal velocity. The new possibilities for improving the dynamic performance of the vehicle are exploited by introducing blur modulation. The proposed method is not affected by exposure time and does not use GPS or any vehicle dynamics model. Therefore, it could easily be used in applications such as mobile robots or autonomous ground vehicles driving on highways with tire slippage.

VII. DISCUSSIONS AND FUTURE WORKS

There also exists a limitation of our study in terms of preventing damage to a camera. Keeping the lens clean from smoke and mud, and blocking small stones flying to the lens should be marked. For example, a fixed inclination line is observed every time when a lens is scratched by a stone. In our observation, however, the effect of a fixed inclination line will have no effect because the number of inclinations in a scene generated by MMB is dominant compared with a just single line generated by the scratch.

The cam mechanism modulating the camera system was proposed to validate the feasibility of the proposed system. However, the new modulation mechanism with high bandwidth, such as voice coil motor (VCM) modulating a lens with optimum modulation speed, should be proposed. The VCM can be a solution for not only obtaining accurate velocity but for reducing the effect of vibration as well. Additionally, the effect of the vehicle vibration should be analyzed in a general term with the experimental results.

REFERENCES

- [1] A. Y. Ungoren and H. Peng, "A study on lateral speed estimation methods," *Int. J. Veh. Auton. Syst.*, vol. 2, no. 1/2, pp. 126–144, 2004.
- [2] M. Stefan, K. Ghorbal, and A. Platzer, "On provably safe obstacle avoidance for autonomous robotic ground vehicles," *Robot., Sci. Syst.*, vol. 9, pp. 104–111, 2013.
- [3] W. Cho, J. Choi, C. Kim, S. Choi, and K. Yi, "Unified chassis control for improvement of agility, maneuverability, and lateral stability," *IEEE Trans. Veh. Technol.*, vol. 61, no. 3, pp. 1008–1020, Mar. 2012.
- [4] H. Guo, H. Chen, F. Xu, F. Wang, and G. Lu, "Implementation of EKF for vehicle velocities estimation on FPGA," *IEEE Trans. Ind. Electron.*, vol. 60, no. 9, pp. 3823–3835, Sep. 2013.
- [5] K. Jo, K. Chu, and M. Sunwoo, "Interacting multiple model Filter-Based sensor fusion of GPS with In-Vehicle sensors for real-time vehicle positioning," *IEEE Trans. Intell. Transp. Syst.*, vol. 13, no. 1, pp. 329–343, Mar. 2012.
- [6] A. S. Huang *et al.*, "Visual odometry and mapping for autonomous flight using an RGB-D camera," in *Proc. Int. Symp. Robot. Res.*, Flagstaff, AZ, USA, pp. 1–16, Aug. 2011.
- [7] H. Du, N. Zhang, and G. Dong, "Stabilizing vehicle lateral dynamics with considerations of parameter uncertainties and control saturation through robust yaw control," *IEEE Trans. Veh. Technol.*, vol. 59, no. 5, pp. 2593–2597, Jun. 2010.
- [8] B. Kitt, A. Geiger, and H. Lategahn, "Visual odometry based on stereo image sequences with RANSAC-based outlier rejection scheme," in *Proc. IEEE Intell. Veh. Symp.*, pp. 486–492, 2010.
- [9] M. Persson, T. Piccini, M. Felsberg, and R. Mester, "Robust stereo visual odometry from monocular techniques," in *Proc. IEEE Intell. Veh. Symp.*, Jun. 2015, pp. 686–691.
- [10] A. Howard, "Real-time stereo visual odometry for autonomous ground vehicles," in *Proc. IEEE Int. Conf. Intell. Robot. Syst.*, 2008, pp. 3946–3952.
- [11] S. Choi, J. H. Joung, W. Yu, and J. Cho, "What does ground tell us? Monocular visual odometry under planar motion constraint," in *Proc. Conf. Robot. Autom.*, Oct. 26–29, 2011, pp. 1480–1485.
- [12] F. Fraundorfer and D. Scaramuzza, "Visual odometry: Part II—Matching, robustness, and applications," *IEEE Robot. Autom. Mag.*, vol. 19, no. 2, pp. 78–90, Jun. 2012.
- [13] B. Lee, K. Daniilidis, and D. D. Lee, "Online self-supervised monocular visual odometry for ground vehicles," in *Proc. IEEE Int. Conf. Robot. Autom.*, 2015, pp. 5232–5238.
- [14] R. Siddiqui and S. Khatibi, "Robust visual odometry estimation of road vehicle from dominant surfaces for large-scale mapping," *IET Intell. Transp. Syst.*, vol. 9, no. 3, pp. 314–322, 2015.
- [15] G. Costante, M. Mancini, P. Valigi, and T. A. Ciarfuglia, "Exploring representation learning with CNNs for frame-to-frame ego-motion estimation," *IEEE Robot. Autom. Mag.*, vol. 1, no. 1, pp. 18–25, Jan. 2016.
- [16] T. Mouats, N. Aouf, A. D. Sappa, C. Aguilera, and R. Toledo, "Multi-spectral stereo odometry," *IEEE Trans. Intell. Transp. Syst.*, vol. 16, no. 3, pp. 1210–1224, Jun. 2015.
- [17] S. Song and M. Chandraker, "Robust scale estimation in real-time monocular SFM for autonomous driving," in *Proc. IEEE Conf. Comput. Vis. Pattern Recog.*, 2014, pp. 1566–1573.
- [18] S. Song, M. Chandraker, and C. C. Guest, "High accuracy monocular SFM and scale correction for autonomous driving," *IEEE Trans. Pattern Anal. Mach. Intell.*, vol. 38, no. 4, pp. 730–743, Apr. 2016.
- [19] M. A. Brubaker, A. Geiger, and R. Urtasun, "Lost! Leveraging the crowd for probabilistic visual self-localization," in *Proc. IEEE Conf. Comput. Vis. Pattern Recog.*, 2013, pp. 3057–3064.
- [20] M. A. Brubaker, A. Geiger, and R. Urtasun, "Map-based probabilistic visual self-localization," *IEEE Trans. Pattern Anal. Mach. Intell.*, vol. 38, no. 4, pp. 652–665, Apr. 2016.
- [21] G. Boracchi, "Estimating the 3D direction of a translating camera from a single motion-blurred image," *Pattern Recog. Lett.*, vol. 30, no. 7, pp. 671–681.
- [22] H. Lin and K. Li, "Motion blur removal and its application to vehicle speed detection," in *Proc. Int. Conf. Image Process.*, 2004, vol. 5, pp. 3407–3410.
- [23] J. Mohammadi, R. Akbari, and M. K. Bahaghighat, "Vehicle speed estimation based on the image motion blur using radon transform," in *Proc. Int. Conf. Signal Process. Syst.*, 2010, pp. 243–247.
- [24] D. Grimaldi, Y. Kurylyak, and F. Lamonaca, "Detection and parameters estimation of locally motion blurred objects," in *Proc. IEEE Int. Conf. Intell. Data Acquisition Adv. Comput. Syst.*, 2011, pp. 15–17.
- [25] A. Levin, P. Sand, T. S. Cho, F. Durand, and W. T. Freeman, "Motion-invariant photography," *ACM Trans. Graph.*, vol. 27, no. 3, pp. 1–9, 2008.
- [26] T. Cho, A. Levin, F. Durand, and W. Freeman, "Motion blur removal with orthogonal parabolic exposures," in *Proc. Int. Conf. Comput. Photogr.*, 2010, pp. 1–8.
- [27] T. Hayakawa, T. Watanabe, and M. Ishikawa, "Real-time high-speed motion blur compensation system based on back-and-forth motion control of galvanometer mirror," *Opt. Exp.*, vol. 23, no. 22, pp. 31648–31661, 2015.
- [28] R. Siegwart, I. Nourbakhsh, and D. Scaramuzza, *Introduction to Autonomous Mobile Robots*. Cambridge, MA, USA: MIT Press, 2011.
- [29] J. Illingworth and J. Kittler, "A survey of the Hough transform," *Comput. Vis., Graph. Image Process.*, vol. 44, pp. 87–116, 1988.
- [30] J.-F. Cai, H. Ji, C. Liu, and Z. Shen, "Framelet-based blind motion deblurring from a single image," *IEEE Trans. Image Process.*, vol. 21, no. 2, pp. 562–572, Feb. 2012.
- [31] J. P. Oliveira, M. A. T. Figueiredo, and J. M. Bioucas-Dias, "Parametric blur estimation for blind restoration of natural images: Linear motion and out-of-focus," *IEEE Trans. Image Process.*, vol. 23, no. 1, pp. 466–477, Jan. 2014.
- [32] H. Tokoro, M. Kawafuku, and M. Iwasaki, "An application of state feedback control to actual vehicle vibration suppression," in *Proc. Adv. Motion Contr. Workshop*, 2014, pp. 185–190.
- [33] A. Geiger, P. Lenz, and R. Urtasun, "Are we ready for autonomous driving? The KITTI vision benchmark suite," in *Proc. IEEE Conf. Comput. Vis. Pattern Recog.*, 2012, pp. 3354–3361.



Minyoung Lee (M'13) received the B.S. and M.S. degrees in mechanical and system design engineering from Hongik University, Mapo-gu, South Korea, in 2010 and 2012, respectively. He is currently working toward the Ph.D. degree with the Cho Chun Shik Graduate School for Green Transportation, Korea Advanced Institute of Science and Technology, Daejeon, South Korea.

His current research interests include sensor fusion, image processing, and vehicle dynamics.



Kyung-Soo Kim (M'00) received B.S., M.S., and Ph.D. degrees in mechanical engineering from Korea Advanced Institute of Science and Technology (KAIST), Daejeon, South Korea, in 1993, 1995, and 1999, respectively.

He was a Chief Researcher with LG Electronics, Inc., from 1999 to 2003, and a DVD Group Manager with STMicroelectronics Company, Ltd., from 2003 to 2005. In 2005, he joined the Department of Mechanical Engineering, Korea Polytechnic University, Siheung, South Korea, as a Faculty Member. Since 2007, he has been with the Department of Mechanical Engineering, KAIST. He serves as an Associate Editor of the *Automatica* and the *Journal of Mechanical Science and Technology*. His research interests include control theory, sensor and actuator design, and robot manipulator design.



Soohyun Kim received the B.S. degree in mechanical engineering from Seoul National University, Seoul, South Korea, in 1978; the M.S. degree from Korea Advanced Institute of Science and Technology (KAIST), Daejeon, South Korea, in 1980; and the Ph.D. degree from Imperial College London, London, U.K., in 1991.

He is currently a Professor of mechanical engineering with KAIST. His research interests include microactuation, miniature mechanisms, precision mechanisms, and optical methods for micro/nanomotion sensing and control.